University of Crete, Department of Physics

I.E.S.L. -F.O.R.T.H.

Photonic Materials & Devices Laboratory

"Optical Fiber Bragg Grating Sensors for Structural Health Monitoring of Wood based Structures"

A thesis submitted for the degree of Bachelor of Science in Physics

by

Anastasia Vantaraki ph5589

Supervisor: Dr. Stavros Pissadakis

Heraklion, Crete

June 2024

FOUNDATION FOR RESEARCH AND TECHNOLOGY - HELLAS

Table of Contents

Acknowledgements

Abbreviations

FBG Fiber Bragg Grating

SMF Single Mode Fiber

MMF Multi Mode Fiber

OSA Optical Spectrum Analyzer

SLED Superluminescent Laser Diode

UV Ultra Violet

Chapter 1

1.1 Introduction

While the first attempts to draw glass into fiber form dates back to Roman times, the first optical fibers were developed in the 1970s so to fill the need of signal transmission with less attenuation and interference compared to other wire media (i.e. copper wires). The last revolutionized the field of telecommunications as it allowed high quality and long distance signal transmission. Silica glass was introduced as it has some favorable properties such as transmission over a wide wavelength range, spanning from the ultra violet to infrared spectral bands. Also silica glass can be doped with a diverse range of ions to modify its optical properties. Optical fibers are now used in telecommunications, sensing in diverse types of fields, light delivery and illumination and quantum optics.

1.2 Optical fiber sensors

The need for monitoring the progress and dynamics of processes in time led people to create sensors. Optical fiber sensors specifically, contrary to other types of sensors have the benefit of having high physical and chemical durability and also being minimally invasive. They are also compact, precise and cost-effective sensing platforms that can be used to detect a variety of physical quantities. Optical fiber sensors can detect changes in temperature[1], strain [1], humidity [2], concentration of selected chemicals [3], sound [4], pressure [5], pH levels [6], and biological quantities (when coated with specific bio sensitive materials. A specific type of optical fiber sensors are based on Bragg gratings. Fiber Bragg gratings (FBGs) are periodic modulations of the refractive index within the core of an optical fiber which produces wavelength specific dielectric mirrors, thus narrow band light reflection.
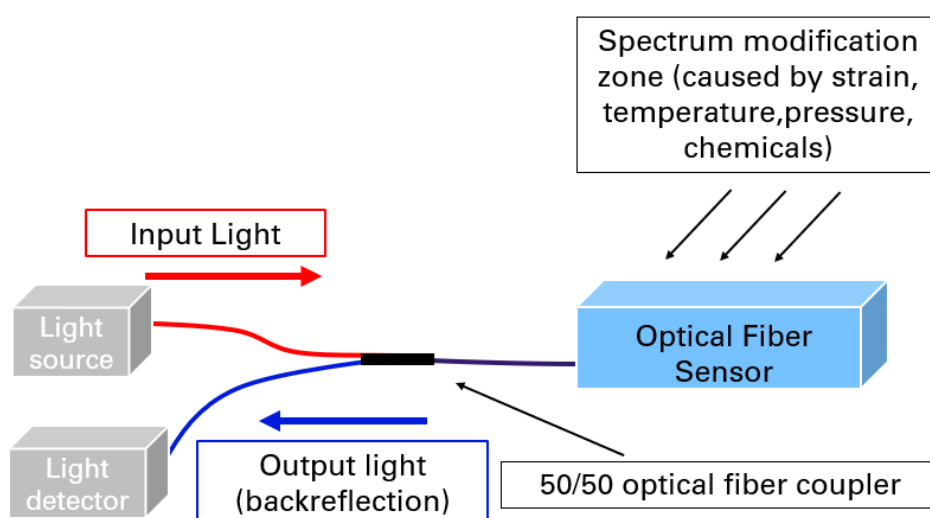

Figure 2-1 Principle of operation of FBG optical fiber sensor

FBGs respond to the externally applied perturbations by exhibiting shifts in the Bragg wavelength and/or strength. The response of the perturbation is received as a amplitude, polarization or phase modulation of the input light of an optical source. The signal is then send in an Optical Spectrum Analyzer (OSA) and measured, for being correlated with the magnitude of the perturbation.

The first FBG as mentioned above was manufactured by K.Hill and this team, with internal inscription using an Argon ion laser [1]. Light from the laser, was coupled into a photosensitive optical fiber core and as the incident laser light interfered with the reflected (around 4%) component, at the high intensity points, a permanent change in the refractive index of the core was observed. A refractive index modulation of the core with the same periodicity with the interference patterns was observed, and thus the first FBG was created.

In this thesis the FBGs that were inscribed and used, were externally inscribed, using the phase mask technique, while using an ArF excimer laser source operating at 193 nm.

1.3 Motivation of this thesis

There has been a lot of interest in the use of optical fiber sensors in the monitoring of the structural health and dynamics in wood based structures [7]. In particular there has been a need for the implementation of optical fiber sensing probes in trees, for monitoring their growth dynamics (Dendrometry) versus weather conditions and agricultural practices (watering, fertilization, etc). Also, there is practical and industrial interest in the implementation of optical fiber sensors in wood based structures for accessing their structural health versus weather and environmental conditions, especially that of humidity and exposure to water.

In this thesis we are performing preliminary investigations on the development of optical sensing probes based on optical fiber Bragg gratings, with potential applications in Dendrometry and wood structures assessment. Two sensing configurations are examined: a flexible belt made of PDMS containing a FBG for potential application in dendrometric applications (see Figure 2-2); and a ring-attached FBG for application in the monitoring of the expansion dynamics due to water exposure of cylindrical wood structures.

Figure 2-2 Proposed positioning of the two sensors developed in the present thesis

Both examples are examined experimentally and upon case are validated using simple theoretical approaches. We anticipate that the sensing platforms developed in this thesis can find applications in agriculture (dendrometry) and wooden structures construction.

1.4 Thesis outline

The theoretical background and equations regarding the optical fibers and FBGs are provided in Chapter 2, as well as Shrink fitting theory. In Chapter 3, the experimental setup that was used and the process and apparatus used are presented. That is, initially the fabrication process and setup of the FBGs .Also the experimental setup used to simulate a tree branch and trunk for the curvature sensor as the set up and also the sample that was used to monitor shrink fit. In Chapter 4, the experimental results of both the sensors are presented and discussed. Finally, in Chapter 4, conclusions and future potential applications are provided.

Chapter 2

2. Theoretical background

In this chapter, basic information about the structure and principles of operation of optical fibers will be discussed. Later fundamental theory regarding the FBGs and also the principles behind the FBG inscription will be presented. Coupled mode theory is also deployed to study the reflectivity and other elementary quantities. Finally a brief introduction to basic formulas of shrink fit theory are also provided.

2.1 Optical fibers

Typically, optical fibers are made of from silica glass and occasionally doped with materials like Germanium dioxide to modify their refractive index and change other properties such as the absorption coefficient and viscosity. They consist of a central core with diameter varying from 8 μm to 10 μm and refractive index at n_{core}=1.45213 (for an SMF-28 optical fiber). The core is surrounded by a concentric cladding with refractive index approximately 1% lower than the core, $n_{cladding}$=1.44692 (for an SMF-28 optical fiber). Both the core and the cladding are secured with a protective coating, consisting typically of one or two layers made of cushioning material (such as acrylate). The main reason is to minimize crosstalk caused by neighboring fibers and the loss-increasing micro bending that takes place when fibers are pushed against rough surfaces [8].
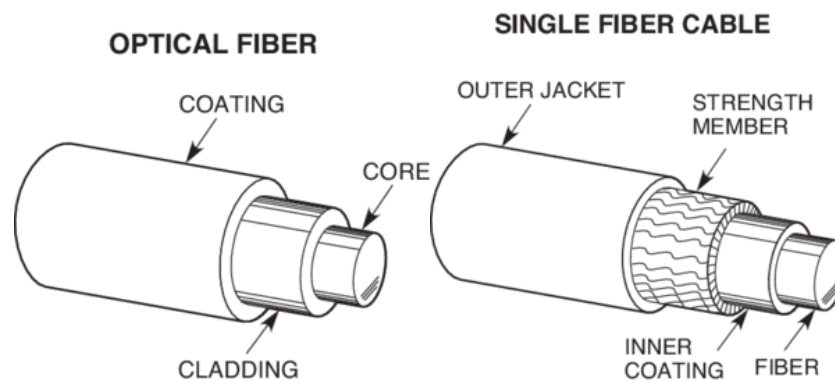

Figure 2-1 Cross section of an optical fiber and a single fiber cable [8]

For even higher protection, it is often to encase the fiber with a polyethylene sheath on top of a strength member.

2.2 Types of optical fibers

Optical fibers depending on their characteristics can be categorized regarding their guiding characteristics [9].
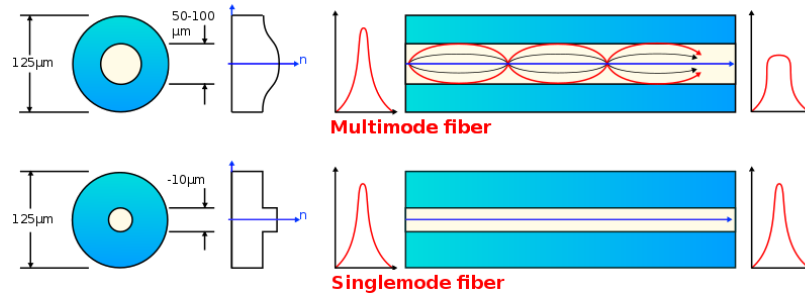
Figure 2-2 How the difference in the diameter of a fiber can affect the way light propagates in the core [9]

In Single Mode Fibers (SMFs), a single mode is guided into the core; for most cases the core has a small diameter of 5 or 10 µm, while the diameter of the cladding is 125 µm. The diameter and refractive index contrast of the core determines how many modes the fiber can support for a specific wavelength. This is the reason why SMFs are suitable for longer communication distances as they have less attenuation and dispersion than Multi-Mode Fibers (MMFs) where several modes are guided for greater core size or refractive index contrast.

An important requirement for the optical fibers is that the length of the cladding is greater than the penetration depth of a guided mode field to prevent the field from reaching the outer boundary of the cladding.

The condition that needs to be followed for light to propagate is the $v < 2.405$ (see Figure 2-10 and Equation (2.20)). The variable v stands for the normalized frequency. When the normalized frequency v is high the optical fibers function as an MMF.

2.3 Principle of operation of optical fibers- Total Internal Reflection

Light transmission in optical fibers is based on the principle of Total Internal Reflection so to confine the light into their core [10].

The refractive index of a material is defined as the ratio between the speed of light in a vacuum to its speed in the material

$$n = \frac{c}{u_{material}} \qquad (2.1)$$

Angle of Incidence (AOI)
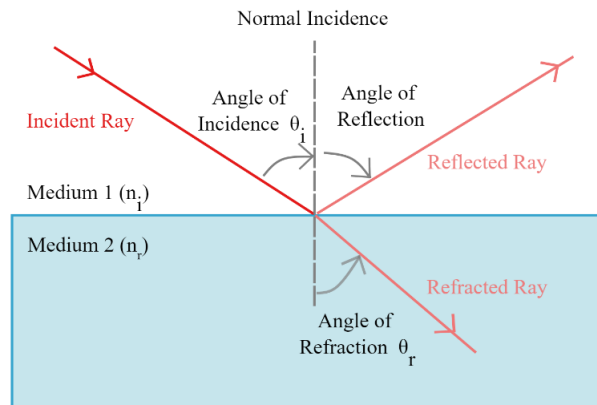
Figure 2-3 Angles of incidence, reflection and refraction [10]

According to Snell's Law, when a light ray is transmitted from one medium to another, the relation between the angle of incidence θ_i and the angle of refraction θ_r is

$$n_i \sin(\theta_i) = n_r \sin(\theta_r). \qquad (2.2)$$

A special case of this law is when a light beam is traveling from a medium with higher refractive index to a medium with a lower refractive index. In that instance, the refracted angle is greater than the incident angle and there is a point where the incident angle is increasing the refracted angle reaches 90 degrees.

Critical Angle and Total Internal Reflection

Figure 2-4 Two special cases of Snell's law [10]

This specific incident angle is known as the critical angle. When the incident angle surpasses the critical angle, light is no longer refracted out of the higher index material, resulting in total internal reflection.

Figure 2-5 Diagram explaining the TIR occurring in an optical fiber [11]
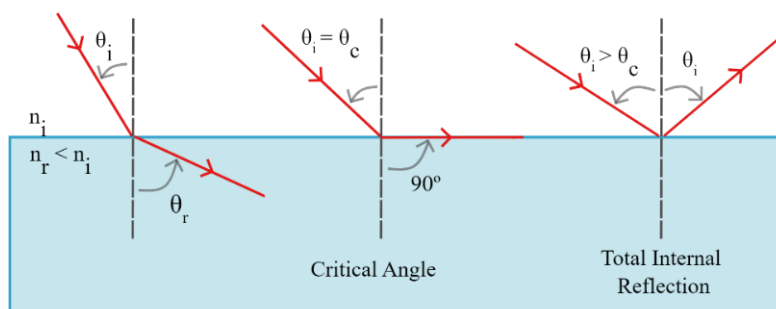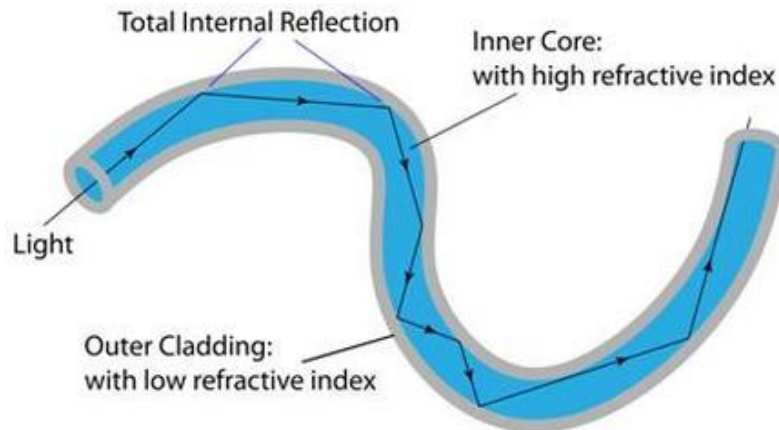
The path of light within the optical fiber is illustrated in the figure above. Despite the Total Internal Reflection, attenuation exists in SMF-28 fibers and a maximum value is approximately 0.17 dB/km at 1550 nm [1] .

2.4 Optical Fiber Bragg Gratings

Fiber Bragg Gratings are structures inside an optical fiber that consist of periodically refractive index variations inside the core of the fiber [1]. The FBGs used in this experiment are also named reflectors. When broadband light is coupled into the core of the fiber, these structures act like a wavelength-specific dielectric mirror.
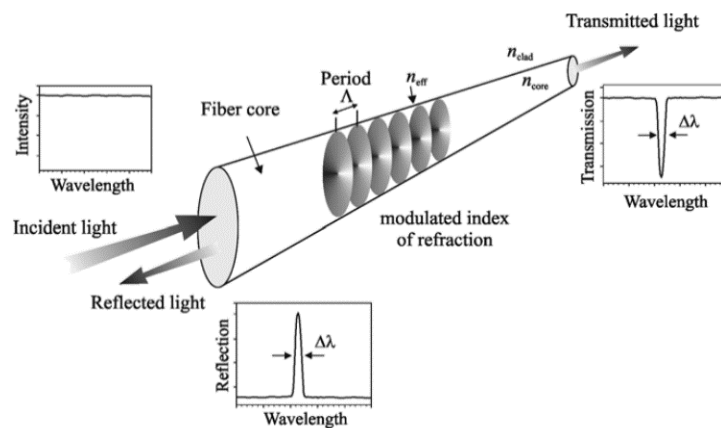
Figure 2-6 Schematic of a FBG inscribed in the core of an optical fiber. Part of the input light is reflected regarding the Bragg condition, while the rest is transmitted [1]

Part of the input light is reflected (Bragg condition) and the remaining is transmitted. The bandwidth of the reflected and transmitted light depends on the length and refractive index modulation of the Bragg grating.

Uniform fiber gratings are characterized by phase fronts perpendicular to the fiber's longitudinal axis, with planes that also have a constant period. As light is guided along the core of the optical fiber, it will be scattered by each grating plane. Only if the Bragg condition is satisfied, will the light be reflected from each of the

contributing planes. In the case that the condition is not satisfied the light will experience very weak reflection at each of the grating planes due to index mismatch and will accumulate along the length of the grating. For instance, a grating with length 1 mm at 1500 nm with $\Delta n \sim 10^{-3}$ will reflect ~ 0.05 % of the off-resonance incident light at wavelengths considerably distant from the Bragg wavelength. Further, it is worth to be mentioned that FBGs reflect radiation not only into back-travelling guided mode, but also into cladding modes and radiation modes (in shorter wavelengths than the λ_B). Since the last modes are not back-guided in the core, they are only observed in transmission and not reflection.
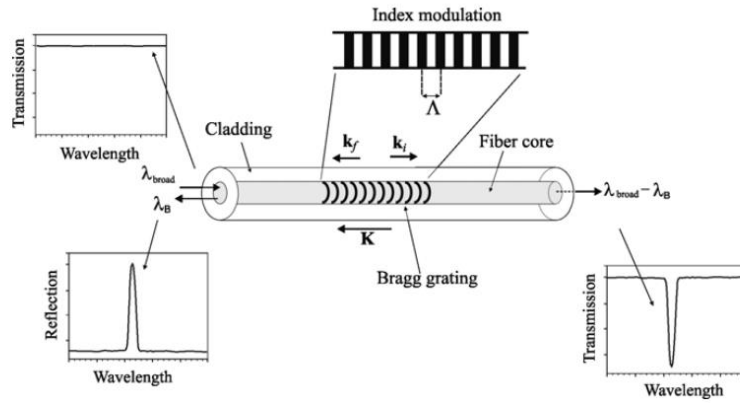
Figure 2-7 Schematic of a uniform FBG with constant index of modulation amplitude and period. Incident, diffracted and grating's wavevectors are shown [1]

The Bragg condition is a result of both the conservation of energy and momentum. Energy conservation

$$\hbar\omega_i = \hbar\omega_f \qquad (2.3)$$

implies that the frequency of the incident and reflected radiation remains the same yet not the vector direction. Momentum conservation states that the wavevector of the incident wave k_i plus the wavevector of the grating K must be equal to the wavevector of the scattered wave k_f

$$k_i + \mathrm{K} = k_f \qquad (2.4)$$

The scattered wavevector is equal in magnitude to the incident one, but with opposite direction. The wavevector of the grating is

$$K = 2\pi / \Lambda \qquad (2.5)$$

where Λ is the spacing of the grating. So, if we substitute the (2.5) we get

$$2\left[\frac{2\pi n_{eff}}{\lambda_{\mathrm{B}}}\right] = \frac{2\pi}{\Lambda} \qquad (2.6)$$

that implies the Bragg condition

$$\lambda_{\mathrm{B}} = 2n_{eff}\Lambda \qquad (2.7)$$

Inside the core of optical fiber with refractive index n_o, the refractive index of the grating varies periodically regarding the following relation

$$\text{n}(z) = n_o + \Delta n \cos\left(\frac{2\pi z}{\Lambda}\right) \quad (2.8)$$

with z being the longitude distance inside the fiber and Δn the amplitude of the induced refracted index (typically $10^{-5} to\ 10^{-3}$).

Wavelength dependent reflectivity is typical of the FBGs. This occurs because when the fiber is subjected to temperature and strain perturbations, it is both the grating plane and its host glass material, modifying the phase matching condition, leading to wavelength dependent reflectivity. Typically for FBGs at 1500 nm the shift response to strain is approximately $1\ pm/\mu\varepsilon$ and in temperature about $(10-15)pm/°C$. Strain ε is a dimensionless quantity defined as the change of a length to the length

$$\varepsilon = \frac{\Delta L}{L} \quad (2.9)$$

Sensitivity to temperature is intrinsic to FBGs. The reason for this is the variation of the silica refraction index induced by thermo-optic effect.

The characteristic of Bragg wavelength shifting is what makes FBGs ideally suited for sensing applications. By monitoring the shift in the Bragg wavelength, one can acquire information about various environmental changes surrounding the FBG. Using the total differential of the Bragg condition (2.7), the shift with respect to strain and temperature can be found.

$$\Delta\lambda_\text{B} = 2\left[\Lambda\frac{\partial n_{eff}}{\partial l} + n_{eff}\frac{\partial\Lambda}{\partial l}\right]dl + 2\left[\Lambda\frac{\partial n_{eff}}{\partial T} + n_{eff}\frac{\partial\Lambda}{\partial T}\right]dT \quad (2.10)$$

The first term corresponds to the change in the induced refractive index and change in the grating spacing in regard to shift, while the latter to the temperature. In equation (2.10) the dependency on the strain can be rewritten as

$$\Delta\lambda_\text{B} = \lambda_B\left[1 - \frac{n^2}{2}\left(p_{12} - v(p_{11} + p_{12})\right)\right]\varepsilon_z \quad (2.11)$$

where p_{11} and p_{12} are components of the strain optic tensor and v is the Poisson's ratio .

2.5 Fabrication of Fiber Bragg Gratings

The fabrication method of FBGs is a crucial part into their following sensing device exploitation, dominating their operational characteristics. Depending on the method used, the FBGs can be characterized as internally or externally written. Internally inscribed are not as practical as the latter, as they require for their construction complex processes . Also, the process of writing inside the fiber with high energy can affect its overall durability.

While there are many techniques to externally write an FBG, the method based on phase mask diffractive interferometry is the most common and advantageous. A phase mask is a thin (Raman-Nath) relief, transmission grating, manufactured from

high quality fused silica transparent to the UV writing beam. The major characteristic of the phase mask is the specific depth of the grating grooves, which in accordance to the refractive index of the mask material for a specific wavelength, fully suppress the 0th order of diffraction, thus, allowing near field interference of the m±1 diffraction orders.
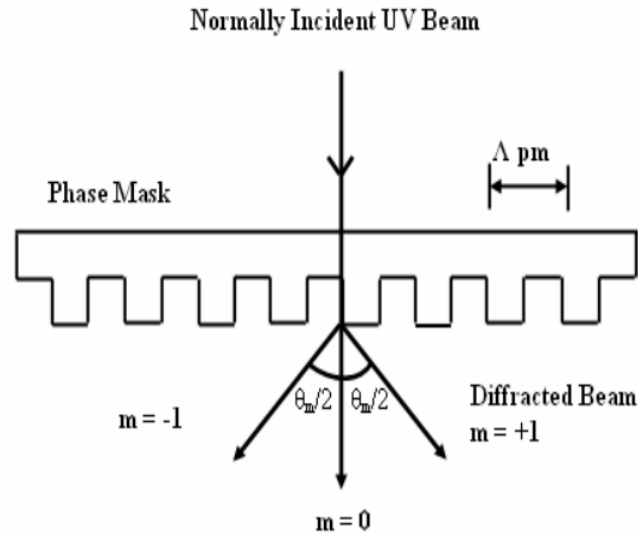

Figure 2-8 Schematic of UV radiation at normal incidence of the phase mask [13]

Practically, when the UV beam is incident to the phase mask the zero-order ($m = 0$) diffracted beam is typically less than 5% of the total transmitted power. The plus and minus diffracted orders ($m = \pm 1$) are maximized with each of them at about 35% of the transmitted power. The interference pattern of the two beams (the $m = \pm 1$) when it is brought together it has a period of the grating Λ_g associated to the diffraction angle $\frac{\theta_m}{2}$ [13] by

$$\Lambda_g = \frac{\lambda_{uv}}{2 \sin\left(\frac{\theta_m}{2}\right)} = \frac{\Lambda_{pm}}{2} \qquad (2.12)$$

where Λ_{pm} is the period of the phase mask that is used and λ_{uv} the wavelength of the UV laser. The period of the inscribed grating is determined by the required Bragg wavelength λ_B for the grating in the fiber which is

$$\Lambda_g = \frac{N\lambda_B}{2n_{eff}} = \frac{\Lambda_{pm}}{2} \qquad (2.13)$$

In this equation, N > 1 is an integer expressing the grating period and n_{eff} is the effective refractive index of the fibers core also including the Bragg condition
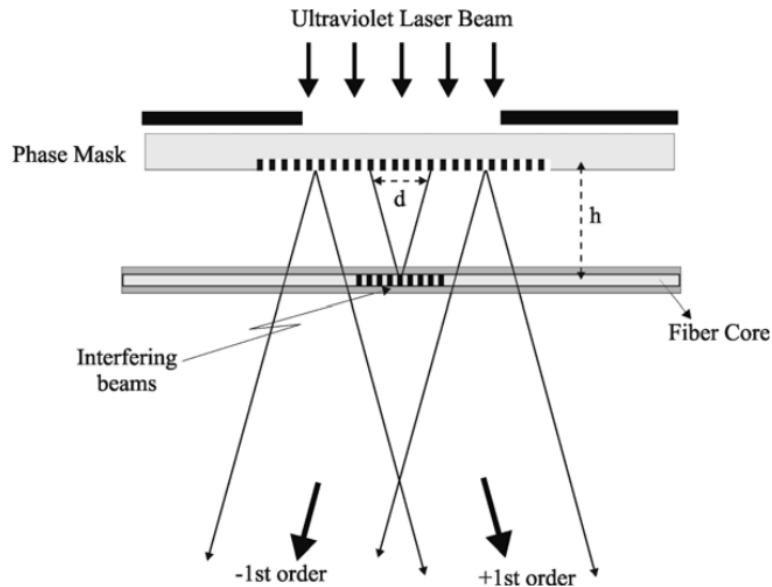
$$\lambda_B = 2n_{eff}\Lambda_g.$$

Figure 2-9 Schematic of phase mask geometry during the inscription of FBGs in optical fibers [1]

While the distance (h) of the fiber to the phase mask is identical for both the interfering beams (m=±1), when h is increasing the separation between the two beams increases too. For this reason, it is crucial for the distance h, not to exceed the spatial coherence of the incident UV beam as the interference fringe contrast will dilute.

2.6 Optical waveguides and fibers

Waveguides are double boundary structures that guide light (E/M radiation) by restricting the transmission of energy solely in one direction. Optical fibers are cylindrical optical waveguides. Optical fibers are optical guidance structures which are made of dielectric materials with high permittivity and thus have a higher refractive index than the surrounding medium. As absolute permittivity ϵ is

$$\epsilon = \epsilon_r \epsilon_o \qquad (2.14)$$

where ϵ_r is the relative permittivity of a material and ϵ_o the permittivity of vacuum [14]. The refractive index of the material is

$$n = \sqrt{(\epsilon_r \mu_r)} \qquad (2.15)$$

for most nonmagnetic materials $\mu_r \sim 1$.

Although Maxwell's equations have exact solutions for the dielectric cylinder specific approximations must be assumed so to access a modal solution for such a type of waveguides [15]. We shall consider that the waveguides are weakly guiding and by that we assume that they have a small index step between the core and the cladding

$$\Delta = \frac{n_{core} - n_{cladding}}{n_{cladding}} \ll 1 \quad (2.16)$$

In this way, we can construct modes whose transverse field is polarized in one direction. We also assume that the cladding area is extending to infinity. The propagation constant $\beta = n\frac{2\pi}{\lambda}$ of any mode is bounded in the interval

$$n_{core}k \geq \beta \geq n_{cladding}k \quad (2.17)$$

with k being the wavenumber of free space.

We also define the modal core parameter u and cladding w

$$u = a(k^2 n_{core}^2 - \beta^2)^{1/2} \quad (2.18)$$

$$w = a(\beta^2 - k^2 n_{cladding}^2)^{1/2} \quad (2.19)$$

The quadratic summation of the above, leads to a third parameter, the normalized frequency v

$$v = ak(n_{core}^2 - n_{cladding}^2)^{1/2} \quad (2.20)$$

Without going into much detail, in cylindrical coordinates the longitudinal (z) and transverse (φ) field components are the following

$$
\begin{aligned}
E_z = -\frac{iE_l}{2ka}\Bigg[& \frac{u}{n_{core}}\frac{J_{l+1}(ur/a)}{J_l(u)}\sin(l+1)\varphi \\
& + \frac{u}{n_{core}}\frac{J_{l-1}(ur/a)}{J_l(u)}\sin(l-1)\varphi \\
& + \frac{w}{n_{cladding}}\frac{K_{l+1}(wr/a)}{K_l(w)}\sin(l+1)\varphi \\
& - \frac{w}{n_{cladding}}\frac{K_{l-1}(wr/a)}{K_l(w)}\sin(l-1)\varphi \Bigg]
\end{aligned}
\quad (2.21)
$$

$$
\begin{aligned}
H_z = -\frac{iE_l}{2kZ_o a}\Bigg[& u\frac{J_{l+1}(ur/a)}{J_l(u)}\cos(l+1)\varphi \\
& - u\frac{J_{l-1}(ur/a)}{J_l(u)}\cos(l-1)\varphi \\
& + w\frac{K_{l+1}(wr/a)}{K_l(w)}\cos(l+1)\varphi \\
& + \frac{K_{l-1}(wr/a)}{K_l(w)}\cos(l-1)\varphi \Bigg]
\end{aligned}
\quad (2.22)
$$

$$E_\varphi = \frac{1}{2} E_t \left(\begin{matrix} J_l(ur/a)/J_l(u) \\ K_l(wr/a)/K_l(w) \end{matrix} \right) [\cos(l+1) + \cos(l-1)\,\varphi] \qquad (2.23)$$

$$H_\varphi = -\frac{1}{2}\frac{E_l}{Z_o} \left(\begin{matrix} n_{core} J_l(ur/a)/J_l(u) \\ n_{cladding}\, K_l(wr/a)/K_l(w) \end{matrix} \right) [\sin(l+1) - \sin(l-1)\,\varphi] \qquad (2.24)$$

The Z_o is the plane wave impedance in vacuum and E_l the electric field strength at the core- cladding interface. With $J_l(ur/a)$ is symbolized the Bessel function that describes the modal field inside the core and with $K_l(wr/a)$, the Henkel function, that describe the modal field outside the core.

As the refractive index step Δ is considered small, the longitudinal components are small compared to the transverse components and so the modes are supposed as linearly polarized LP.

By setting $n_{core} = n_{cladding}$ in equations from (2.21) to (2.24) we obtain the characteristic equation for the LP modes

$$u\frac{J_{l-1}(u)}{J_{l(u)}} = -w\frac{K_{l-1}(w)}{K_l(w)} \qquad (2.25)$$

Using $v^2 = u^2 + w^2$, equation (2.25) becomes

$$\frac{du}{dv} = \frac{u}{v}[1 - k_1(w)] \qquad (2.26)$$

where $k_l(w) = K_l^2(w)/K_{l-1}(w)\,K_{l+1}(w)$. Using appropriate approximations we can obtain $u(v)$ for all modes, while for higher order modes we have

$$u(v) = \frac{u_o \exp\left[arc\sin(s/u_{cutoff}) - \arcsin(s/u)\right]}{s} \qquad (2.27)$$

with $s = \left(u_{cutoff}^2 - l^2 - 1\right)^{1/2}$, where u_{cutoff} is the cutoff value of u.

For the LP_{01} mode the u parameter becomes

$$u(v) = \left(1 + \sqrt{2}\right)v/\left[1 + (4 + v^4)^{\frac{1}{4}}\right] \qquad (2.28)$$

With equation (2.28) and (2.18) we are able to calculate the propagation constant β. To make the calculation independent of the fibers configuration, we shall work on the ratio

$$b(v) = 1 - (u^2/v^2) = [(\beta^2/\kappa^2) - n_{cladding}^2]/(n_{core}^2 - n_{cladding}^2) \qquad (2.29)$$

which, for small index difference becomes

$$b \approx \frac{\beta/k - n}{n_{core} - n_{cladding}} \qquad (2.30)$$

Finally from equation (2.16) and (2.30) we obtain

$$\beta(v) = n_{cladding} \ (b\Delta + 1) = nk[1 + \Delta - \Delta(u^2/v^2)] \quad (2.31)$$

By plotting the normalized propagation constant $\beta(v)$ we can conclude that the LP_{01} can only propagate for a specific range of values of the normalized frequency v ,starting from 0 to about 2.405.
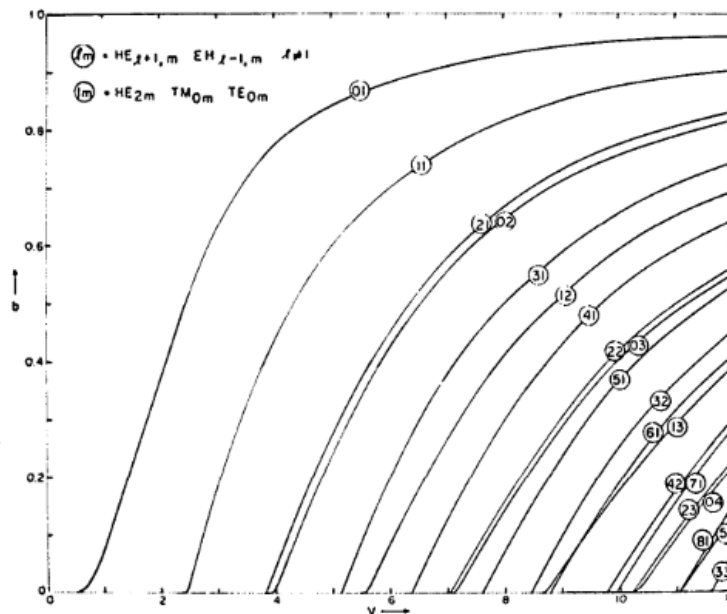

Figure 2-10 Normalized propagation parameter b=(β/k-n)/(n_{core}-n_{cladding}) as a function of the normalized frequency v [15]

Overall, the v number is a useful quantity for a fiber, as a fiber with a low v number is sensitive to micro-bend and modal expansion losses. For v values below $v \approx 2.045$, a fiber can only support one mode per polarization direction (Single Mode Fibers).

2.7 Coupled mode theory

In order to study the optical filters (included Bragg reflectors) and perturbations in optical fibers, coupled mode theory needs to be deployed. This analysis requires to make the following approximations : 1) there is no absorption loss 2) the propagating modes do not couple with the TE and TM radiation modes and 3) the waveguide is weakly guiding $\Delta \ll 1$ (2.16) [16].

The cylindrical coordinates are used

$$\frac{\partial^2 \Psi}{\partial r^2} + \frac{1}{r}\frac{\partial \Psi}{\partial r} + \frac{1}{r^2}\frac{\partial^2 \Psi}{\partial \varphi^2} + \frac{\partial^2 \Psi}{\partial z^2} + n_i^2 k^2 = 0 \qquad (2.32)$$

where $n_i = n_{core}, n_{cladding}$ and $k = 2\pi/\lambda$, the free space propagation constant (wavenumber). Assuming that the solution is

$$\Psi(r, \varphi, z, t) = F(r) \cos(v\varphi) \exp[i(\omega t - \beta z)] \quad (2.33)$$

letting that n_i is uniform along z axis. Substitution of (2.33) to (2.32) gives the eigen fiends $\mathcal{E}_v$ and H_v.

Assuming also that the SMF has an index profile

$$\epsilon(z) = \begin{cases} [n_o^2 + \Delta\epsilon \cos(\theta z)] & in\ core\ region \\ n_o^2 & in\ cladding\ region \end{cases} \quad (2.34)$$

Where n_o^2 is the index of a uniform fiber, $\Delta\epsilon$ the induced index perturbation, $\theta = 2\pi/\Lambda$ and Λ the perturbation period, gives the expansion of the perturbated fields

$$E = \sum_{v=1}^{N} a_v \mathcal{E}_v \quad (2.35)$$

$$H = \sum_{v=1}^{N} b_v \mathcal{H}_v \quad (2.36)$$

In the above a_v and b_v are the mode amplitudes and N is the number of modes in the fiber. Substituting (2.34), (2.35) and (2.36) to (2.32) and assuming that the transverse coupling coefficient is much larger than the longitudinal we can calculate a set of the following coupled differential equations

$$\frac{dC_\mu^+}{dz} = \frac{\Omega}{i} C_\mu^+ \exp(i2\Delta\beta z) \quad (2.37)$$

$$\frac{dC_\mu^-}{dz} = \frac{\Omega}{i} C_\mu^+ \exp(-i2\Delta\beta z) \quad (2.38)$$

in which the + and – indicate the forward and backward traveling waves. Also C_μ^- and C_μ^+ are the normalized amplitudes of the fields , $\Delta\beta = \beta - \pi/\Lambda$ and

$\Omega = \left(\frac{\Delta\epsilon\omega\epsilon_o}{8P}\right) \int_0^a \int_0^{2\pi} \mathcal{E}_v^2 r\ dr\ d\varphi$. Solving these differential equations with boundary conditions $C^+(0) = 1$ and $C^-(L) = 0$ with L being the length of the filter, gives

$$C^+(z) = \frac{-\exp(i\Delta\beta z)}{[\Delta\beta \sinh(SL) - iS \cosh(SL)]} \{\Delta\beta \sinh[S(z - L)] + iS \cosh[S(s - L)]\} \quad (2.39)$$

$$C^-(z) = \frac{\Omega \exp(-i\Delta\beta z)}{[\sinh(SL) - iS\cosh(SL)]}\sinh[S(z-L)] \qquad (2.40)$$

where $S = (\Omega^2 - \Delta\beta^2)^{1/2}$.

From all the above we can obtain the reflectance and transmittance as a function of wavelength and the length of the filter by using the following ratios

$$R(\lambda, L) = \left|\frac{C^-(0)}{C^+(0)}\right|^2 \qquad (2.41)$$

$$T(\lambda, L) = \left|\frac{C^+(L)}{C^+(0)}\right|^2 \qquad (2.42)$$

. The reflectance can be also categorized, with respect to the coupling coefficient Ω as following

$$R(L, \lambda) = \begin{cases} \dfrac{\Omega^2 \sinh^2(SL)}{\Delta\beta^2 \sinh^2(SL) + S^2 \cosh^2(SL)} & for \ \Omega^2 > \Delta\beta^2 \\ \dfrac{\Omega^2 \sin^2(QL)}{\Delta\beta^2 - \Omega^2 \cos^2(QL)} & for \ \Omega^2 < \Delta\beta^2 \end{cases}$$

in which $Q = (\Delta\beta^2 - \Omega^2)^{1/2} = iS$.

2.8 Shrink fit model

Shrink fit model is a fundamental approach in structural mechanics for fitting together two shafts in a plug mode. In the shrink fit model two cylindrical shafts, one solid (male part of diameter b+δ) and one hollow (female part of diameter b) are fitted either through selective heating of the outer (female) part so to allow insertion of the male part in the out-cladding component. Upon cooling the outer part (female) shrinks and tightly fits to the male part, exerting pressure at the conduct interface which is evaluated through Equation (2.43).

The analysis is based mainly to the approach that the fitted parts have a constant cross section and material (density) during the shrink fit area.
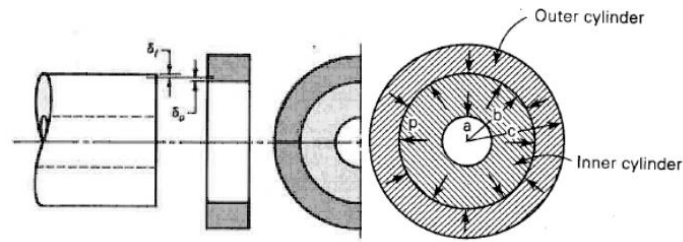
Figure 2-11 Schematic diagram for shrink fit, before and after press fit [17]

The fit develops a pressure determined by the equation [17]

$$P_{shrink\,fit} = \frac{\delta}{2b\left[\frac{1}{E_o}\left(\frac{c^2+b^2}{c^2-b^2}+v_o\right)+\frac{1}{E_i}\left(\frac{b^2+a^2}{b^2-a^2}+v_i\right)\right]} \qquad (2.43)$$

where E_o and E_i is the Youngs modulus of the materials used, while v_o and v_i

the Poisson's ratio. In the following experiment, the radius a is zero, as the fitted object is not hollow and so the expression for the pressure turns into

$$P_{shrink\,fit} = \frac{\delta}{2b\left[\frac{1}{E_o}\left(\frac{c^2+b^2}{c^2-b^2}+v_o\right)+\frac{1}{E_i}(1+v_i)\right]} \qquad (2.44)$$

Let b denote the radius of the shaft and c represent the outer radius of the cylinder. The maximum interference parameter (dimensional) between the shaft and the cylinder is denoted by

$$\delta = shafts\,max\,diamater - hole\,min\,diameter. \qquad (2.45)$$

Chapter 3

3. Experimental

In this chapter, the fabrication setup and inscription process of FBGs in SMF-28 optical fibers will be presented. The development of a sensor designed to measure the growth and overall changes in tree branches and trunks will be explained. Finally, the creation of the sample intended to monitor alterations in wood-based structures and the corresponding sensor development will be presented.

3.1 Bragg grating fabrication setup

The setup that was used in this experiment so to fabricate the FBGs is shown in Figure 3-1Figure 3-1. The laser that was used is an ArF excimer laser with wavelength at 193 nm and pulse duration of 8 ns.

Initially, the beam is redirected by a set of two mirrors into an attenuator that is used for tuning the power of the laser pulses, by allowing only a percent of the total beam to pass through. After that, the beam is focused using a cylindrical lens into a diaphragm that both blocks the unwanted reflections and adjusts the beam's size.
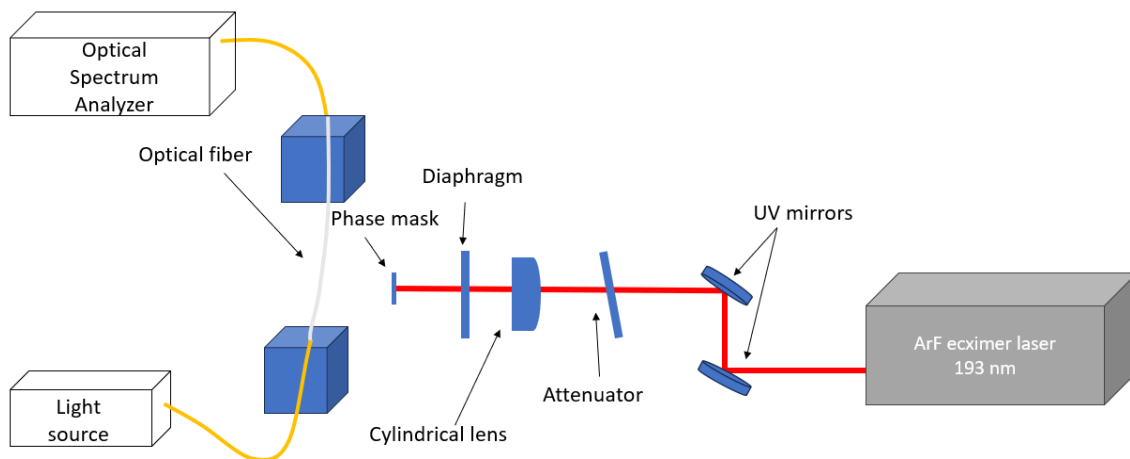

Figure 3-1 Setup used for the fabrication of FBG in an optical fiber

The beam width is 0.5 cm and its height is 0.013 cm. The SMF-28 fiber is fixed by specialty V-grooves and strong magnets, at a specialty fork, kept at a small distance behind the phase mask.
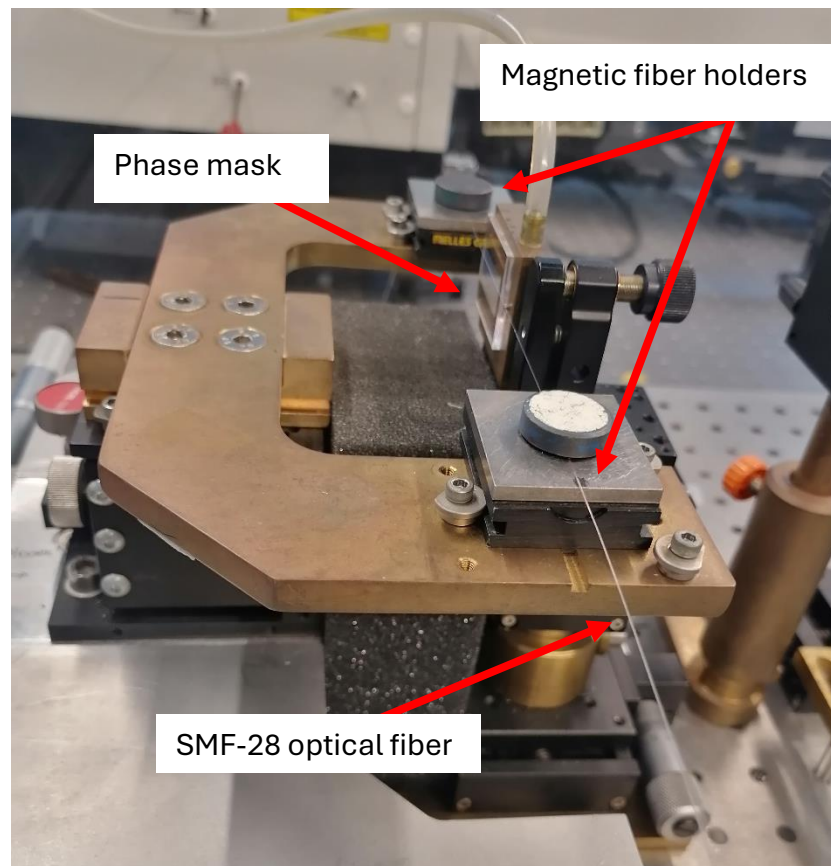
Figure 3-2 Set up used to keep the optical fiber and the phase mask in place during the inscription prosses

The phase mask is attached onto a specialty holder using a vacuum case. The part of the optical fiber that the FBG will be written on, is stripped of its acrylic jacket and cleaned with isopropanol.

To monitor the FBG inscription's progress, we used a DL-BP1-1501A SLED light source with center wavelength 1550 nm [18], connected with the fiber two ends using bare fiber adaptors, so to monitor the transmission spectrum in real time mode during the grating inscription process. For measuring the fiber spectra obtained an ANDO AQ6317b Optical Spectrum Analyzer (OSA) was employed at 0.01 nm resolution.

SMF-28 optical fibers were used for inscribing the Bragg reflectors used in this experiments. Specific characteristics of the SMF-28 optical fiber are presented in the Table 1[12][19].

Characteristics of SMF-28	
Maximum Attenuation at 1550 nm	≤0.17 dB/km
Cladding diameter	≈ 125 µm
Core diameter	8.2 µm
Refractive index difference	0.36%

Table 1 Characteristics of the SMF-28 optical fiber

3.2 Experimental setup and materials for the curvature sensor

In this part the development of the curvature FBG sensor is presented, which is enclosed in a belt of Polydimethylsiloxane (PDMS). Such a sensing probe is expected to be used as an add-on unit on the trunk or branches of trees for monitoring growth rate with respect to agricultural practices and weather conditions. Both the elastic belt fabrication and calibration apparatus are described in this section.

3.2.1 Sample and stage manufacturing

PDMS is a transparent silicone polymer that is created by combining a base and a curing agent. Upon thermal polymerization, it transforms into a viscoelastic material. Sylgard 184 [20] was chosen, as it is ideal for sensing purposes due to its high optical transparency and elasticity.

To construct the platform that the FBG was embedded, a two-pieces mold made of Teflon was used. Teflon was chosen as it can withstand high temperatures, required for the polymerization of the PDMS, without deformations. The two parts of the PDMS were combined with ratios varying between 1:12 and 1:13 and then placed in the Teflon case. Before molding the PDMS silicon oil was applied onto the Teflon mold for easier removal of the solidified belt. The Teflon mold was inserted inside a metal enclosure for uniform heat distribution during polymerization and for holding the two-pieces Teflon mold in place. The curing of the PDMS included heating at a temperature of 40 °C for about 4 hours using a hot plate.
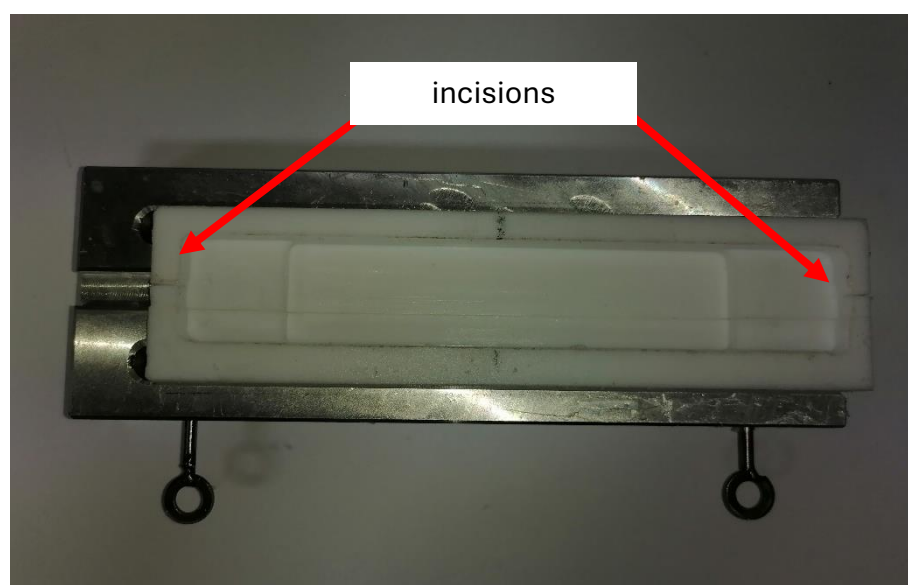

Figure 3-3 Teflon mold used for casting the elastic belt

For accommodating the FBG the Teflon mold contained two incisions/thin slots on each side. After the PDMS belt was polymerized it was removed from the mold and placed in the setup Figure 3-5Figure 3-5.

3.2.2 Calibration apparatus

Since the sensing probe was to be used in dendrometric applications, a specialty apparatus was constructed in the laboratory for calibrating its response (see Figure 3-4).
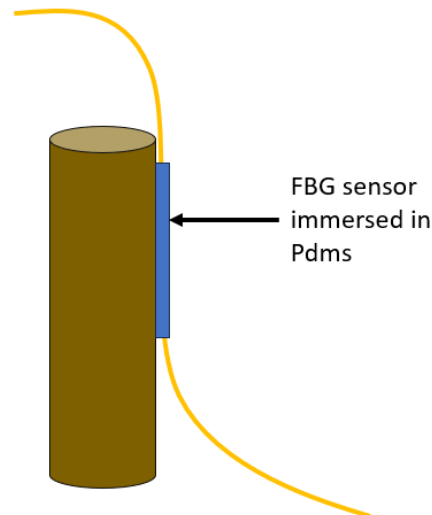

Figure 3-4 Exact placement of the sensing probe in a tree trunk or branch

The two xyz micro blocks where clamped on the metallic platform, as shown in Figure 3-5. One of the micro blocks, was placed on a second micrometric stage allowing for translations greater than 2mm for covering long deformations of the sensor. The last allowed to move the xyz micro block, and simultaneously measure the displacement using the second micrometric stage.
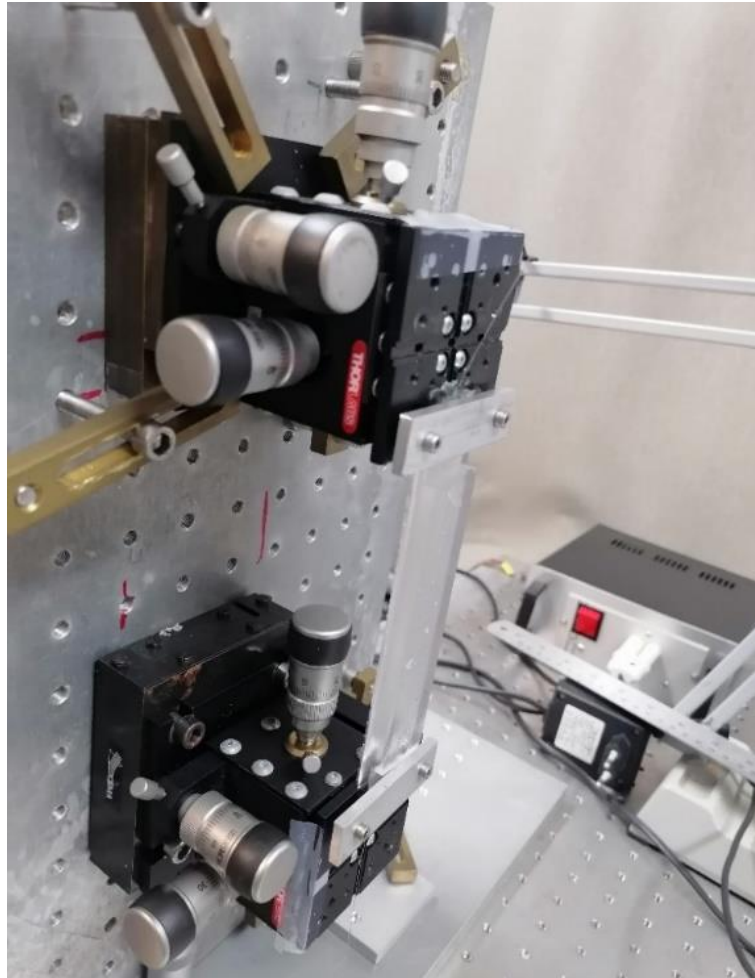
Figure 3-5 Experimental setup for calibrating the elastic belt containing the FBG sensor

In order to test the relation between curvature and shift of the reflection Bragg peaks, the sensor was initially secured in the micro blocks with as low as strain as possible (see left picture in *Figure 3-6*)*Figure 3-6*.
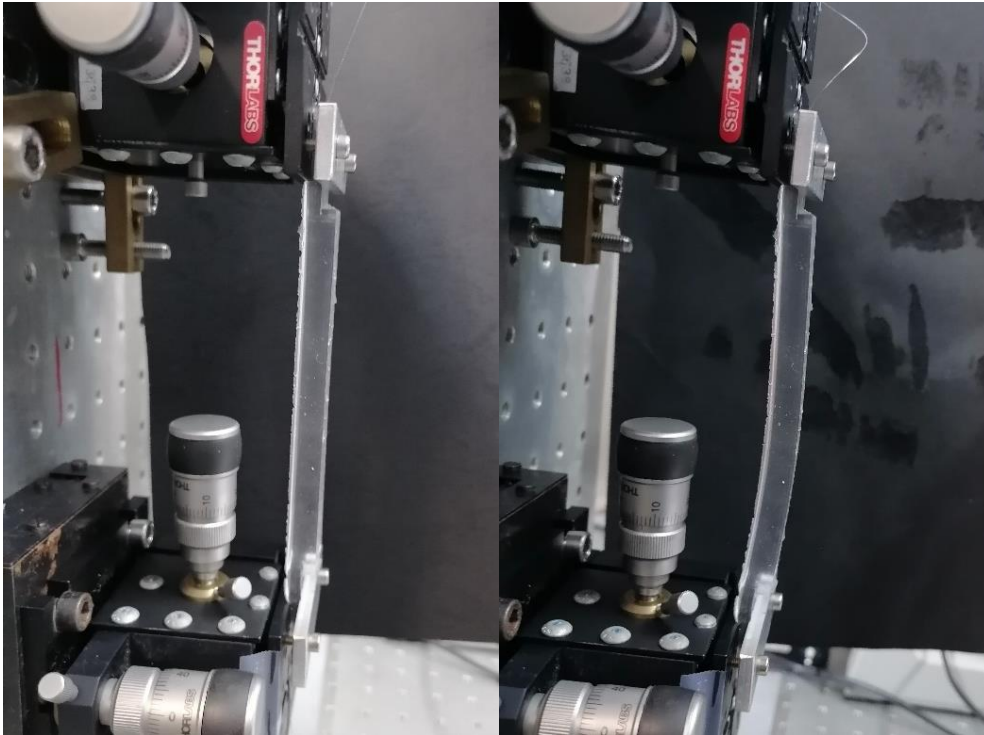
Figure 3-6 Experimental setup for calibrating the elastic belt containing the FBG sensor with a sensing belt loaded under no-strain and under compression strain

The sensor was also tested for its hysteresis performance by increasing the curvature and then decreasing it to reach the initial state. After the hysteresis of the sensing probe was tested, elongation strain was also applied.

3.3 Experimental setup and materials for shrink fit sensor

In order to supervise the structural health and expansion behavior of the wooden shaft, a specialty PVC ring was manufactured for hosting the FBG sensor. Two FBGs of different wavelengths were inscribed in a single optical fiber, one of which was used to monitor the temperature shifts, while the other one to trace the mechanical changes exerted onto the PVC ring.

The two FBGs were inscribed with an energy of $130 \frac{mJ}{cm^2}$, $40\ Hz$ repetition for about 10 min, while using the laser apparatus described above. Masks with different periods were used so as to yield Bragg peaks at distinct wavelengths. The Bragg peak located at approx. 1541nm was used to monitor the spectral shifts due to temperature variation and the peak located at approx. 1553nm was placed in the outer surface of the PVC cylinder, for measuring mechanical deformation due to the change of the diameter of the wooded shaft.

The FBGs were spliced using Fujikura fusion splicer FSM-45S. Pigtail connectors were placed in the end of each optical fiber to ensure stability in connections and to reduce unwanted reflections.

The sample composes of a beech shaft that is inserted in a cylinder made of PVC Figure 3-7Figure 3-7.
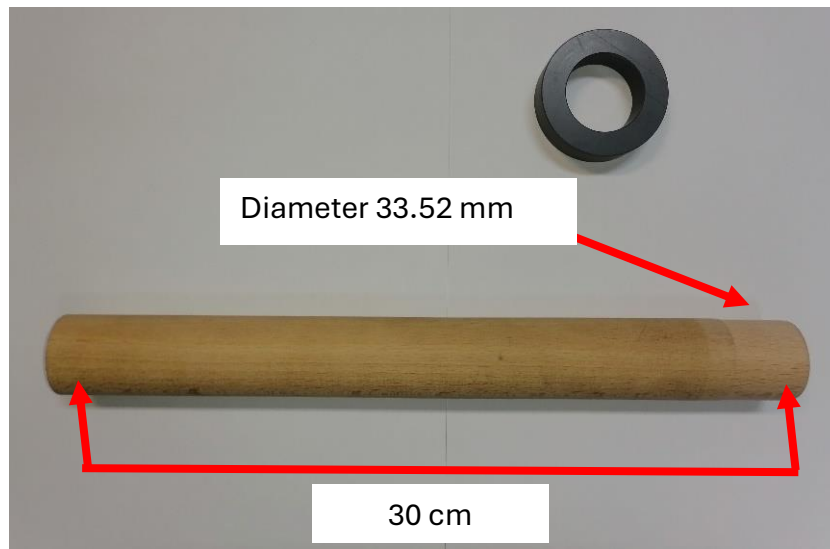

Figure 3-7 Photograph of a beech wood shaft and PVC transduction ring used in the current experiment
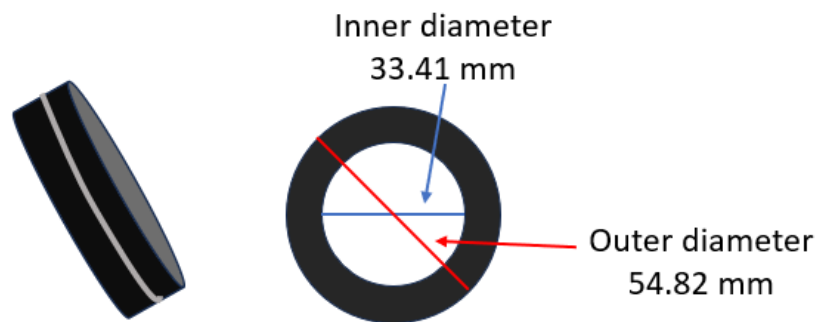

Figure 3-8 Dimensions of the cylinder and the perimetric cut used to secure the optical fiber sensor

The ring was lathed from hard PVC material, having a thickness of 21.41mm, an outer diameter of 54.21mm and an inner diameter of 33.41mm. Also, on the outer perimeter of the PVC ring a shallow slot was engraved for placement of the FBG

sensor Figure 3-8. The FBG sensor was wrapped around the PVC ring and fixed using the specialty X120 optical sensor adhesive suitable for gluing glass with PVC.
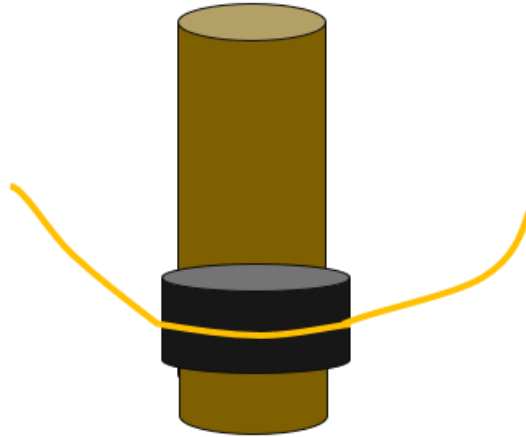

Figure 3-9 Schematic of the sample and the placement of the examined sensor

Figure 3-9 displays the exact placement of the sensor on the wooden sample. The sample was then placed in a box and the reflection spectrum was collected, using a 2x2 50/50 optical fiber coupler, with one end connected to an OSA and the other to SLED light source. The other two ends were connected with the sensor ends as it is shown in Figure 3-10.
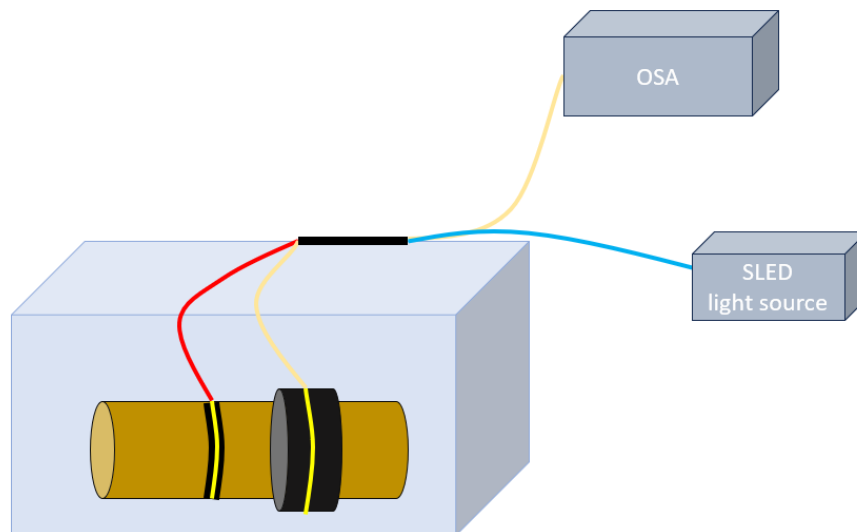

Figure 3-10 Placement of the sample with the sensor connected in the box

The exact setup that was used in the experiment is demonstrated in Figure 3-11. The sample was also connected with a metallic slab so that it will not float.
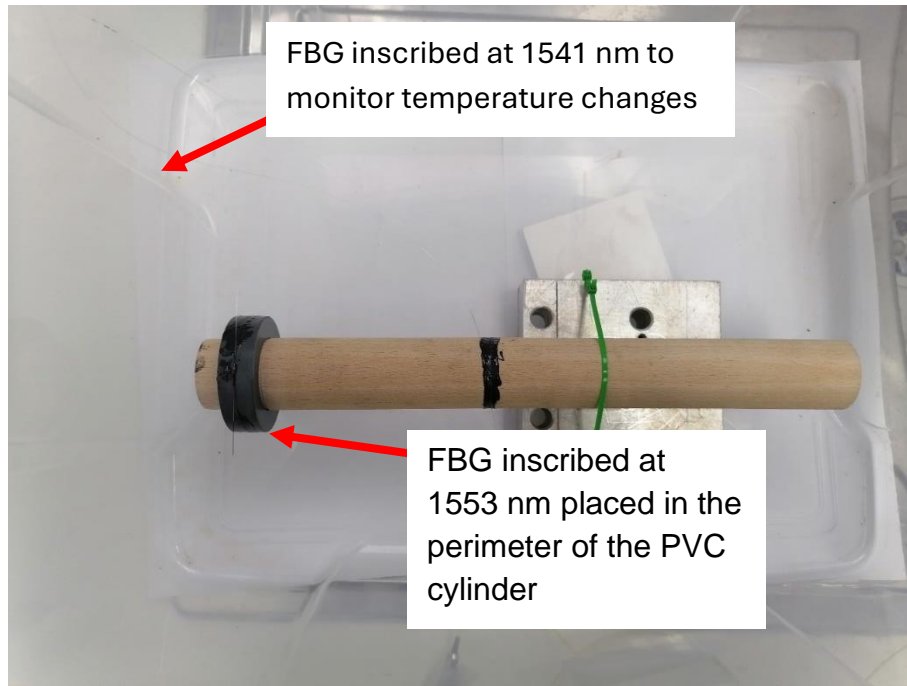
Figure 3-11 Placement of the sample inside the box

In Figure 3-12 is displayed the reflection spectrum of the FBGs after it was placed and secured in the box.
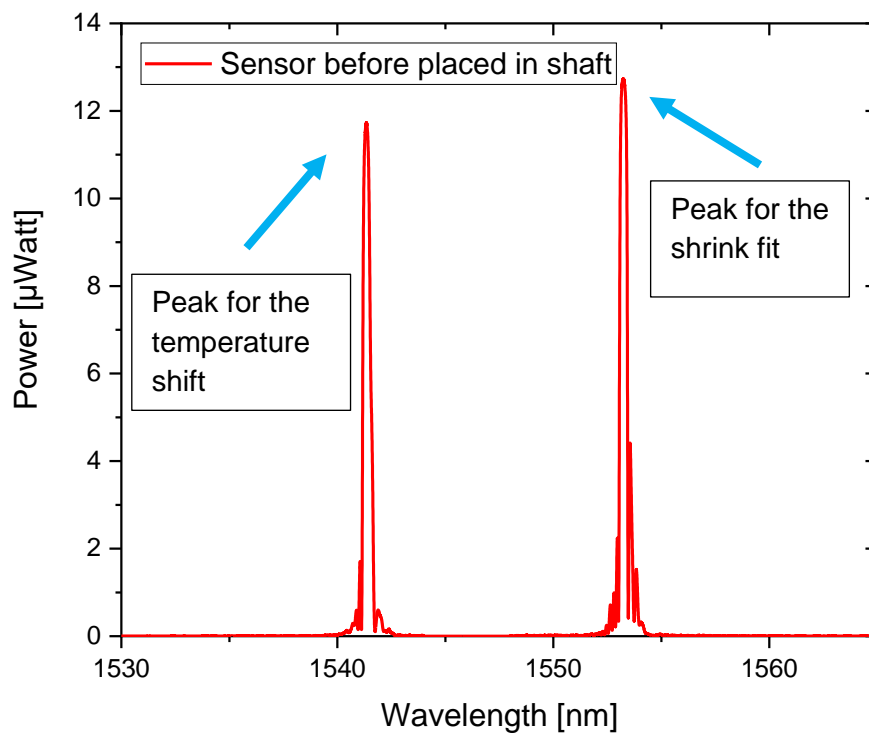

Figure 3-12 Reflection spectrum of the two Bragg peak FBG sensor before installation on the shaft

The reflection spectra after the FBGs were placed on the sample before and after the adhesive was cured are given in Figure 3-13. The 1553 nm peak of the FBG that was placed around the PVC ring shifts to the red; this is might due to the fact that the specialty glue used shrinks under thermal curing.
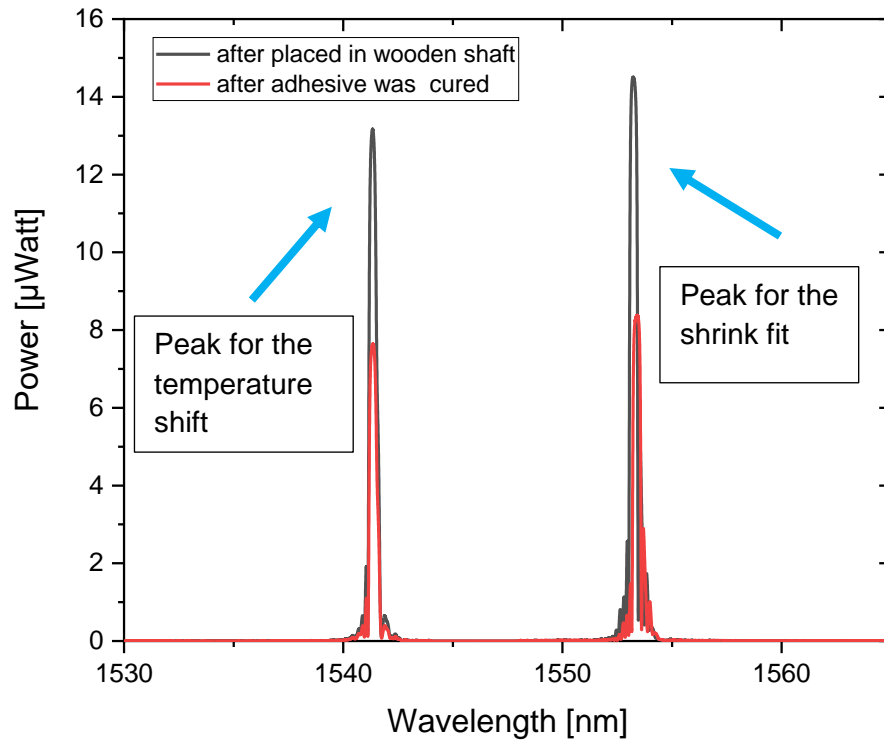

Figure 3-13 Reflection spectra after the placement in the sample, before and after the adhesive was cured.

3.3.1 Measurement procedure

In order to obtain increasing diameter in the beech shaft and subsequently study the shrink fit effect and sensor operation, the complete set (wooden shaft with PVC ring) was immersed in a box filled with water.
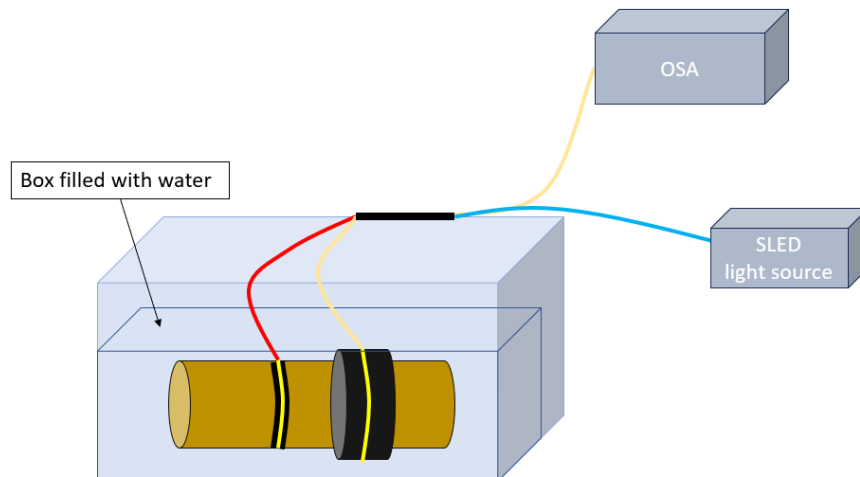
Figure 3-14 Schematic of the setup used to increase the shafts diameters, it consists of a box filled with water and the sample fully immersed in it

As the wooden shaft absorbs water, its diameter increases exerting radial-tangential pressure to the PVC ring that induces deformation in it, measured by the FBG glued onto its circumference

For simplifying the measurements and not perturbing the shaft containing the FBG sensor, two identical wooden shafts were placed under water, the first of which had the sensors connected, while the second one was solely used to measure the diameter changes introduced by water diffusion with an electronic vernier

For better monitoring in real time the spectral shifts of the Bragg peaks of the FBG sensors, a Lab View code was used, programmed so to record the spectrum of the two FBGs every 15 minutes while using the OSA (Spectr. Resolution 0.01 nm, Sensitivity High1). The total duration that the wooden shaft with the PVC ring were immersed into water was ~ 6 hours, followed by ~ 3 hours relaxation of the sensing system outside water so to monitor reversing effects.

The radial pressure that each part applies to the other can be calculated using (2.43 and also Table 2 .

	Young's modulus (GPa)	Poisson's ratio
	E_R	v_{TR}
Beech wood	1.858	0.373
PVC (hard)	3.275	0.429

Table 2 Young's modulus and Poisson's ratio for the materials used [21],[22],[23]

Chapter 4

4. Experimental results

In this section the results of the above experiments will be presented and discussed. For the PDMS belt sensor, transmission spectra were obtained and their shift were analyzed using Origin Lab. As far as, the shrink fitting study, reflection spectra were obtained, together with measurements from the diameter of the wooden shaft and temperature. As the Bragg peaks were too wide to determine the exact peak position with the same error for all the measurements, Gaussian fit was used to determine them using again Origin Lab.

4.1 Discussion for curvature sensor

Initially, the sensor was positioned at the strain apparatus and by monitoring its Bragg wavelength, it was positioned at a no-strain state, namely place "0". Then, the micro block stages were brought in compression mode, returned back to place "0", and then tensile strain was applied. These measurements appear in Figure 4-1. For the compression mode of operation the Bragg peak wavelength was blue-shifting 0.9nm, approximately.
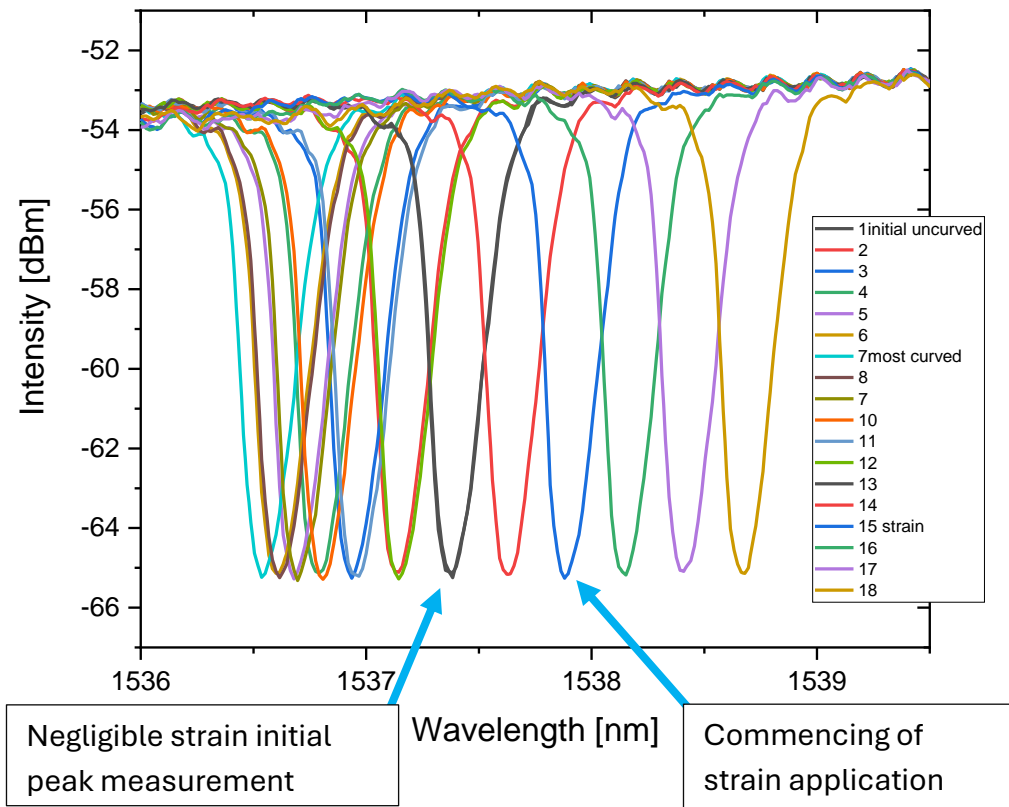

Figure 4-1 Transmission spectra obtained for the belt extendability FBG sensor

The hysteresis of the sensor was also investigated and results are presented in *Figure 4-2*, as for the same displacement the Bragg peak returns in the initial position.
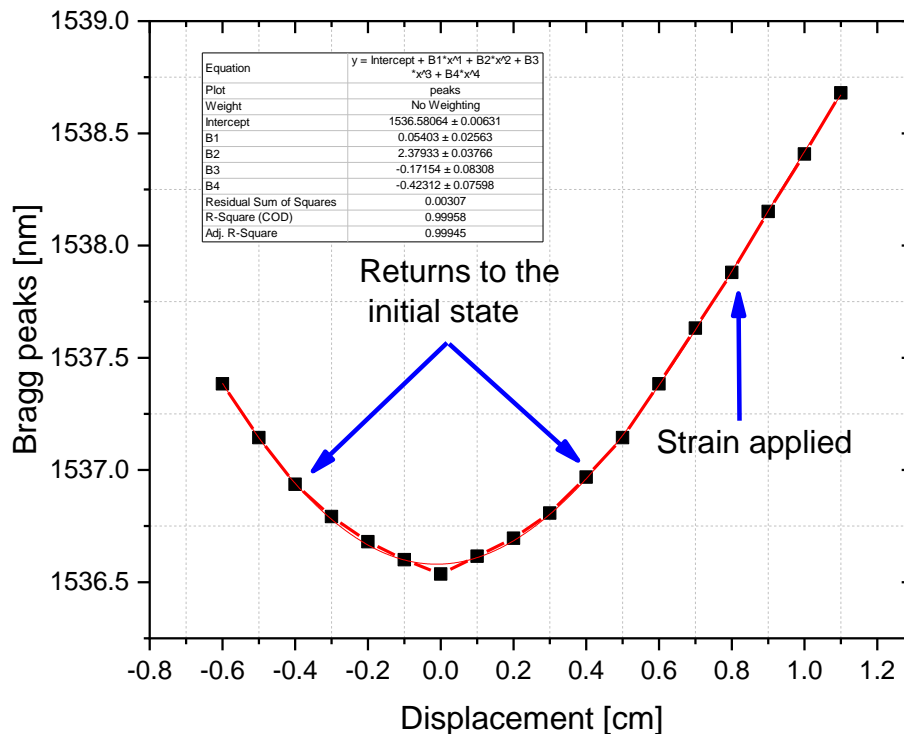

Equation	y = Intercept + B1*x^1 + B2*x^2 + B3 *x^3 + B4*x^4
Plot	peaks
Weight	No Weighting
Intercept	1536.58064 ± 0.00631
B1	0.05403 ± 0.02563
B2	2.37933 ± 0.03766
B3	-0.17154 ± 0.08308
B4	-0.42312 ± 0.07598
Residual Sum of Squares	0.00307
R-Square (COD)	0.99958
Adj. R-Square	0.99945

Figure 4-2 Bragg peaks vs displacement of the micrometric stage obtained for the belt extentability FBG sensor

From the above investigation it was found that the sensor exhibited a sensitivity of 1.95nm/mm, evaluated from the displacement data for the tensile strain applied. It is expected that different types of optical fibers, PDMS polymer and curing conditions and geometry of the belt can lead to greater sensitivities. It is expected that this sensing probe will be soon tested in real field environment, by attaching that onto the trunk of a mid-age tree (20-30 years old), where small growth changes are difficult to be assessed using standard dendrometry techniques in short times (few days).

4.2 Discussion for shrink fit sensor

The wooden shaft with the PVC ring FBG were fully immersed into the water, while the auxiliary FBG was used for monitoring temperature changes. The Bragg grating wavelength shift versus immersion time in the water are presented in Figure 4-3.

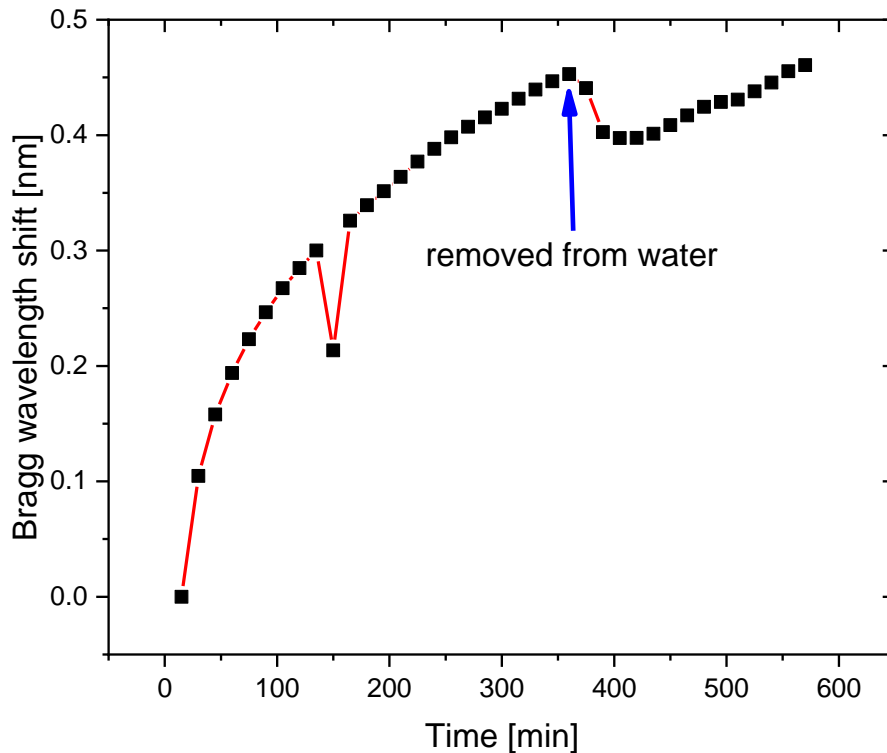These data have been corrected for temperature fluctuations.

Figure 4-3 Bragg wavelength shift vs the time that the sample was placed underwater and during the drying process. The moment that it was removed from water, is denoted

As the sample is placed underwater and the diameter of the shaft is increasing, red shift of the PVC mounted FBG is observed. When the diameter measurements reached a plateau (see Figure 4-4) (at 360 minutes from the beginning of the experiment) the sample was removed from the water and left to dry in ambient air. During that relaxation period, the Bragg grating wavelength peak shown a particular behavior. Initially, a blue shift was observed (~0.05nm), followed by a red shift with slope similar to the one observed at the late stages of water immersion (200-360min). By considering Figure 4-3 and Figure 4-4 we speculate that the particular behavior is attributed to the ongoing in-diffusion of the water into the wood fibers. While the outer layers of the wood shaft may undergo a drying process, the remaining water already absorbed in the wood volume, continues to diffuse into the inner parts of the wood, sustaining volume expansion although of lower magnitude, also manifested in the shrink-fit transducer. In addition, plastic changes may also take place at the interface between of the PVC ring and the X120 optical sensor adhesive, or the glued fiber itself; these assumptions are still under investigation
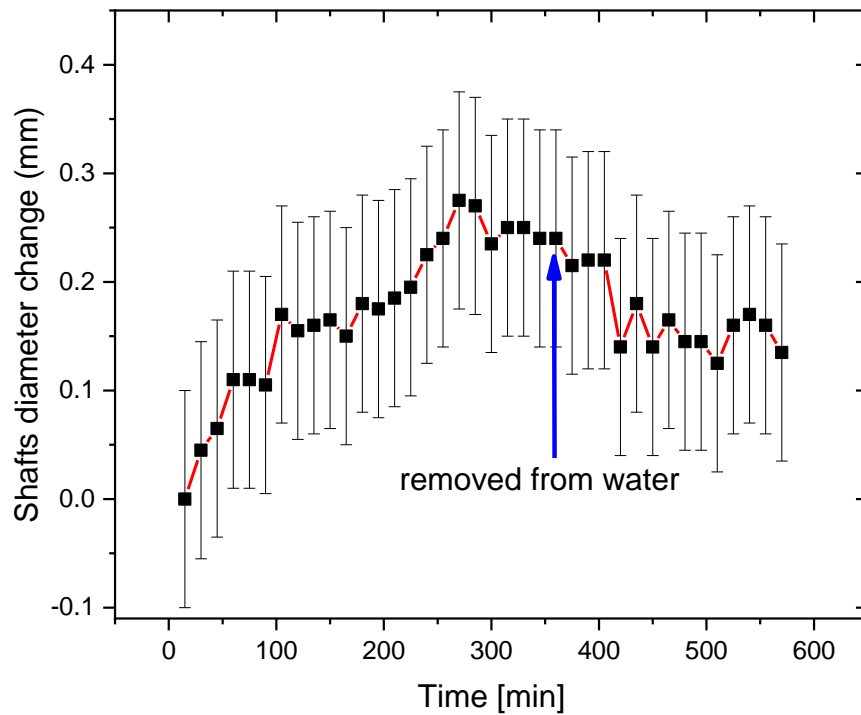
Figure 4-4 Shafts change in diameter vs time that the sample was placed underwater and during the drying process. The moment that it was removed from water, is denoted

It is observed that from Figure 4-5 that as the diameter of the shaft is increasing, the applied pressure is increasing too, as it is expected. By using typical equations for shrink fit model presented in section 2.8, the radial pressure components is elaborated. Maximum pressure of ~ 9MPa are estimated, roughly corresponding to vectoral strains of 2700με.
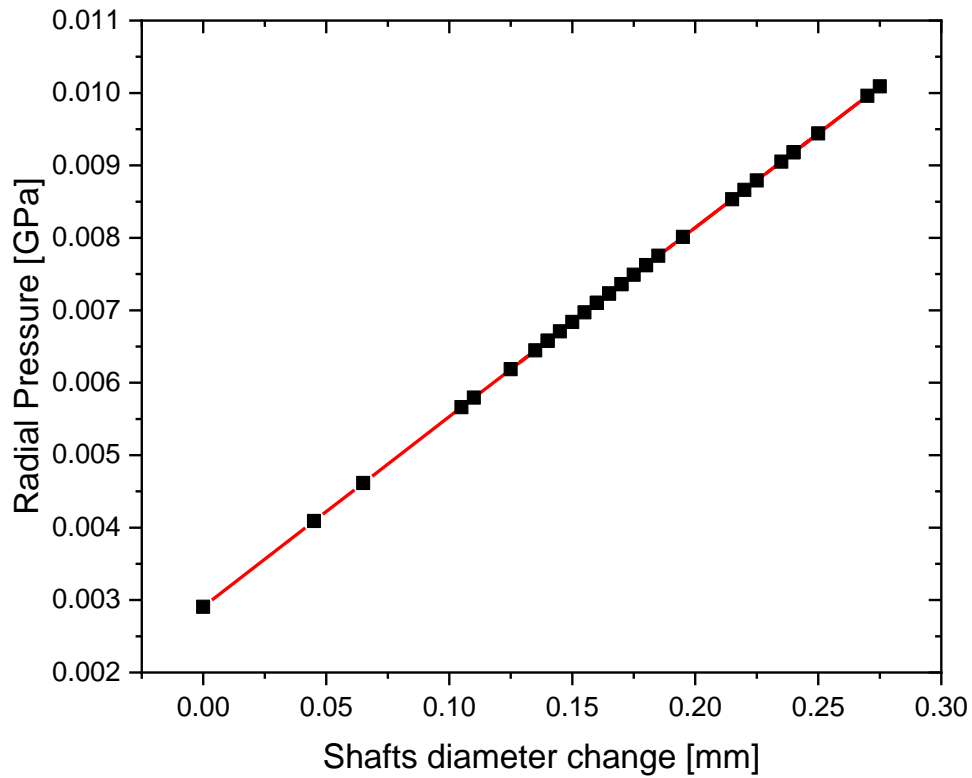
Figure 4-5 Radial Pressure (2.44) vs shafts diameter change during the time that the sample was placed underwater and during the drying process

As far as the relation between the Bragg peaks shift and the change in the diameter of the shaft, initially as the diameter change is increasing, a red shift in the Bragg peak also appears in Figure 4-6.
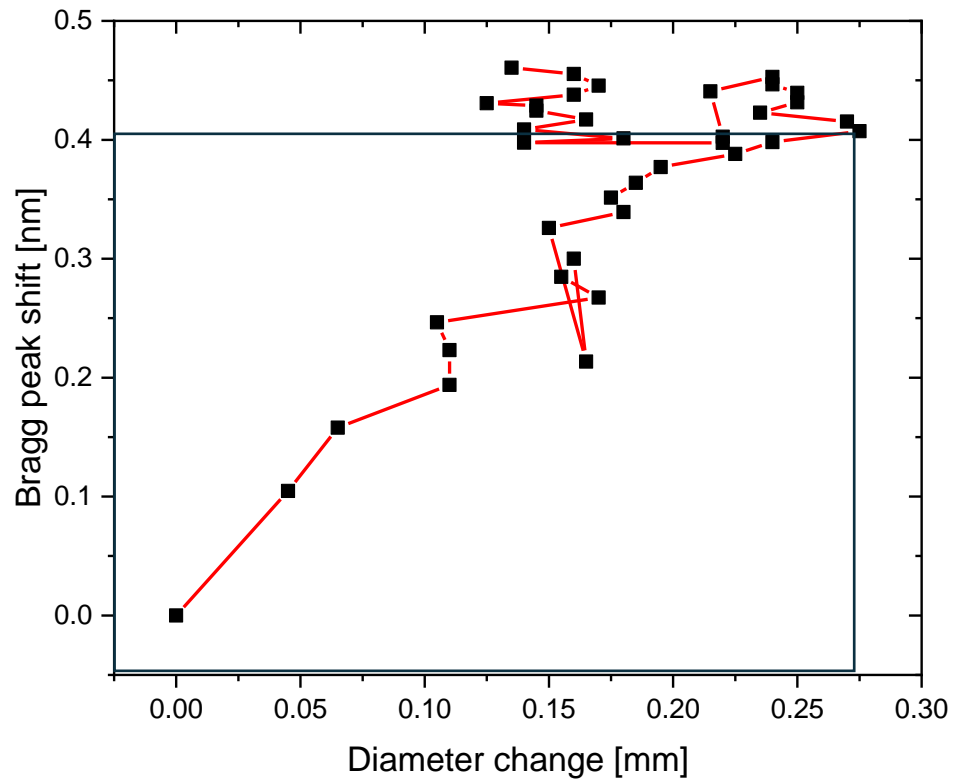
Figure 4-6 Bragg wavelength shift vs Diameter change of the shaft during the time that the sample was placed underwater and during the drying process

Chapter 5

5. Conclusions

In this thesis the development of sensing probes for monitoring wooden based structures while using FBGs was presented. The sensors developed were:

1) An elastic PDMS belt platform encapsulating a FBG for measuring extendibility/displacement, with potential applications in dendrometry
2) A shrink-fit sensor based on a PVC ring sensing transducer with a FBG positioned on its outer circumference for monitoring water swelling of wooden shafts.

The first sensing probe, was based on FBGs and inscribed in SMF-28 optical fiber using 193nm excimer laser radiation and phase mask interferometry. These FBGs were embedded in a PDMS belt made from Sylgard 184 polymer. The PDMS embedded sensing probe was tested in laboratory conditions under different strain and curvature stimulations, for investigating its response under realistic conditions may occur in open field applications. The calibration process shown a 2.144 nm Bragg wavelength shift for a maximum sensor displacement of 1.1mm, leading to a sensitivity figure of 1.95nm/mm. Considering that typical small scale interrogator offer a wavelength resolution of 0.05nm, typical displacements of the order of ~0.2mm can be readily detected. Based on the above sensitivity figure and accounting that typical growth rates for most tree trunks are of the order of 20µm/day, this sensing probe can be used for providing monitoring for typical time intervals spanning between 10 days.

The shrink-fit sensing probe was based on a PVC ring sensing transducer with a FBG glue mounted on its outer circumference. This sensing probe was used for tracing diameter changes in circular shape wooden shafts when they are immersed in water medium. The measurement of the Bragg grating peak wavelength shift versus the change of the diameter of the wooden shaft, allowed an estimation of the sensitivity of the device, estimated at 1.5nm/mm of diameter change. This device was tested also during the relaxation phase of the wooden shaft, when that was removed from the water and partially returned to its initial diameter. Further, the maximum Bragg grating peak wavelength shift of 0.4nm was correlated with tangential stresses of the order of 9.18MPa, computed using standard analytical theory for shrink-fit interaction. This sensing probe allowed the probing of diameter changes lower than 1.0% (~0.8%) in the diameter of the wooden shaft, over a water immersion period of 6 hours. The last set a promising prospect for the use of this sensing probe (or an optimized version) in the tracing of deformation related to humidity or watering in wooden structures in real time; also in dendrometric applications for monitoring growth changes in tree branches.

6. References

[1] Fibre Bragg Gratings. (2006).

https://www.researchgate.net/publication/226100236_Fibre_Bragg_Gratings

[2] Konstantaki, M., Pissadakis, S., Pispas, S., Madamopoulos, N., & Vainos, N. A. (2006). Optical fiber long-period grating humidity sensor with poly(ethylene oxide)/cobalt chloride coating. *Applied Optics*, *45*(19), 4567. https://doi.org/10.1364/ao.45.004567

[3] *Silk Fibroin enabled Optical Fiber Methanol Vapor Sensor.* (2020, May 1). IEEE Journals & Magazine | IEEE Xplore. https://ieeexplore.ieee.org/stamp/stamp.jsp?tp=&arnumber=9044416

[4] *Fiber Optic Sensor for Navy Applications.* (1991). https://www.researchgate.net/publication/3304241_Fiber_Optic_Sensors_for_Navy_Applications

[5] FBGS. (2021, November 29). *Pressure Sensing - FBGS.* https://fbgs.com/solutions/pressure-sensing/

[6] Martínez, J. P. P., Núñez, I. S., Pérez, G. B., Mixcóatl, J. C., Aguirre, S. M., & Merino, R. P. (2007). Optical fiber sensor for the measurement of the pH level using organic dyes deposited by the sol-gel process. *Proceedings of SPIE, the International Society for Optical Engineering/Proceedings of SPIE.* https://doi.org/10.1117/12.742279

[7] Using fibre-optic sensing for non-invasive, continuous dendrometry of mature tree trunks. (n.d.). https://hal.science/hal-04574205/file/Pr%C3%A9print%20Fiber%20optic%20for%20dendrometry.pdf

[8] Fiber Optic Basics. (n.d.). https://www.newport.com/t/fiber-optic-basics

[9] SMF or MMF? And what exactly is dispersion on a glass fiber? (n.d.). BIT. https://www.bit.nl/news/2759/88/SMF-or-MMF-And-what-exactly-is-dispersion-on-a-glass-fiber

[10] MEETOPTICS | Search & Compare quality optics. (n.d.). https://www.meetoptics.com/academy/angle-of-incidence#total-internal-reflection-and-the-critical-angle

[11] How do they work? (n.d.). The Use of Light and Colour in Modern Technology. https://todaystechnologyy.weebly.com/how-do-they-work.html

[12] *Corning SMF-28 Product information*. (2014b).
https://www.corning.com/media/worldwide/coc/documents/Fiber/SMF-28%20ULL.pdf.

[13] Tahir, B., Ali, J., & Rahman, R. A. (2006). Fabrication of fiber grating by phase mask and its sensing application. *ResearchGate*.
https://www.researchgate.net/publication/228678640_Fabrication_of_fiber_grating_by_phase_mask_and_its_sensing_application/link/02e7e515b64d34750c000000/download?_tp=eyJjb250ZXh0Ijp7ImZpcnN0UGFnZSI6InB1YmxpY2F0aW9uIiwicGFnZSI6InB1YmxpY2F0aW9uIn19

[14] Wilson, J., & Hawkes, J. F. B. (1998). *Optoelectronics: An Introduction*. Prentice Hall.

[15] *Optica Publishing Group*. (n.d.). https://opg.optica.org/ao/fulltext.cfm?uri=ao-10-10-2252&id=73014

[16] Lam, D. K. W., & Garside, B. K. (1981). Characterization of single-mode optical fiber filters. *Applied Optics*, *20*(3), 440. https://doi.org/10.1364/ao.20.000440

[17] *ANSYS Non-Linear Multi staging Technique for Shrink Fit Analysis*. (2010). https://heavymovablestructures.org/wp-content/uploads/2017/12/78.pdf

[18] Superluminescent LED Source (with Integrated Optical Circulator). (n.d.). https://ibsen.com/wp-content/uploads/DL-BP1-1501A_RevB.pdf

[19] *Corning SMF-28 Product information*. (2002). http://www.photonics.byu.edu/FiberOpticConnectors.parts/images/smf28.pdf

[20] *SYLGARDTM 184 Silicone Elastomer Kit*. (n.d.). https://www.dow.com/en-us/pdp.sylgard-184-silicone-elastomer-kit.01064291z.html#overview

[21] *Polyvinyl chloride hard | Designerdata*. (n.d.). https://designerdata.nl/materials/plastics/thermo-plastics/polyvinyl-chloride-hard?cookie=YES

[22] *Comparisons of finite element models used to predict bending strength of mortise-and-tenon joints*. (n.d.-b). https://doi.org/10.15376/biores.15.3.5801-5811

[23] Effect of Temperature, Cross-head Speed and Duration of loads on the Mechanical Properties of PVC Polymeric Material. (1999). https://www.researchgate.net/publication/330678648_Effect_of_Temperature_Cross-

head_Speed_and_Duration_of_loads_on_the_Mechanical_Properties_of_PVC_Polymeric_Material

[24] Trantidou, T., Elani, Y., Parsons, E., & Ces, O. (2017). Hydrophilic surface modification of PDMS for droplet microfluidics using a simple, quick, and robust method via PVA deposition. *Microsystems & Nanoengineering, 3*(1). https://doi.org/10.1038/micronano.2016.91

[25] *What is a Fiber Bragg Grating? | FBG | Sensors*. (n.d.). HBK World. https://www.hbkworld.com/en/knowledge/resource-center/articles/strain-measurement-basics/optical-strain-sensor-fundamentals/what-is-a-fiber-bragg-grating

[26] Kennedy, P. (2023, March 6). *+1/-1 order phase masks (FBG) - Ibsen Photonics*. Ibsen Photonics. https://ibsen.com/products/phase-masks/1-1-order-phase-masks-fbg/

[27] *Basic optics for optical fiber*. (n.d.). Fosco Connect. https://www.fiberoptics4sale.com/blogs/archive-posts/95048070-basic-optics-for-optical-fiber